Research Square

Preprints are preliminary reports that have not undergone peer review.
They should not be considered conclusive, used to inform clinical practice,
or referenced by the media as validated information.

Systematic study of total, Coulomb and nuclear breakup cross sections in 8B reactions on medium and heavy targets.

Lucas Vusi Ndala

ndalal@unisa.ac.za

University of South Africa

Mantile Leslie Lekala

University of South Africa

Research Article

Keywords: Total breakup cross section · Coulomb breakup cross section · Nuclear breakup cross section

Posted Date: November 20th, 2026

DOI: https://doi.org/10.21203/rs.3.rs-11521462/v1

License: This work is licensed under a Creative Commons Attribution 4.0 International License.
Read Full License

Additional Declarations: No competing interests reported.

Noname manuscript No.
(will be inserted by the editor)

Systematic study of total, Coulomb and nuclear breakup cross sections in ^{8}B reactions on medium and heavy targets.

L. V. Ndala · M. L. Lekala

Received: date / Accepted: date

Abstract The breakup dynamics of the weakly bound proton-rich nucleus ^{8}B on ^{58}Ni and ^{120}Sn targets are investigated within the Continuum Discretized Coupled Channels (CDCC) framework. The elastic scattering angular distributions are compared with available experimental data to assess the reliability of the adopted reaction model. The total, Coulomb, and nuclear breakup cross sections are calculated to examine the interplay between nuclear and Coulomb interactions and to investigate the effects of continuum continuum couplings (CCC). The results reveal that the relative contributions of nuclear and Coulomb breakup depend on the target and incident energy. The inclusion of CCC substantially suppresses the total and nuclear breakup cross sections, whereas the Coulomb breakup cross section is comparatively less affected. Their influence is also reflected in the angular distributions, with calculations excluding CCC exhibiting extended angular distributions and pronounced oscillatory behavior for the heavier target. Convergence tests show that the calculated breakup observables are stable with respect to the maximum continuum-bin energy, $\varepsilon_{\max}$, over the investigated range. The multipole analysis further demonstrates that contributions beyond $\lambda_{\max}$=2 remain non negligible and that multipoles up to λ=6 are needed to obtain converged results within the adopted model space. These findings highlight the importance of continuum couplings and higher multipole contributions in describing the breakup of ^{8}B on medium-mass and heavy targets.

Keywords Total breakup cross section · Coulomb breakup cross section · Nuclear breakup cross section

L. V. Ndala
Department of Physics,
University of South Africa,
Private Bag X6, Florida 1710,
Johannesburg, South Africa
E-mail: ndalal@unisa.ac.za

1 Introduction

The breakup of weakly bound nuclei has attracted considerable theoretical and experimental interest over the past several decades, owing to its importance in understanding nuclear structure and reaction dynamics [1–10]. In particular, halo nuclei, characterized by an extended valence-nucleon distribution and a small separation energy, are highly susceptible to breakup during collisions with target nuclei. The proton-halo nucleus ^{8}B is particularly interesting because its valence proton has a separation energy of approximately 0.137 MeV. This weak binding makes its breakup dynamics sensitive to both the nuclear and Coulomb interactions with the target. The interplay between these interactions provides an opportunity to investigate the relative contributions of nuclear and Coulomb breakup and their interference in reactions involving weakly bound nuclei.

The breakup dynamics of ^{8}B have been investigated experimentally and theoretically for several target nuclei [11–13]. For the ^{8}B+^{58}Ni system, breakup measurements near the Coulomb barrier have been reported at different incident energies [14, 15], with ^{7}Be detected as a breakup fragment. Continuum-discretized coupled-channels (CDCC) calculations were subsequently employed to analyze the measured breakup cross sections and investigate the role of projectile continuum states in the reaction dynamics. These studies established the importance of coupling to the breakup continuum in describing the interaction of the weakly bound ^{8}B projectile with the target.

Further investigations of $^{8}\mathrm{B}+^{58}\mathrm{Ni}$ have examined the influence of breakup couplings on elastic scattering and reaction cross sections near the Coulomb barrier. Comparisons between experimental measurements and theoretical calculations have provided insight into the effects of the weak binding of ^{8}B on the reaction dynamics. These studies demonstrate that the coupling between the elastic channel and the projectile continuum can influence the scattering observables and must be considered when describing reactions involving this proton-halo nucleus.

The role of continuum-continuum couplings (CCC) in the breakup of ^{8}B has also been investigated [16]. In particular, the effects of diagonal and off-diagonal CCC were examined for the $^{8}\mathrm{B}+^{58}\mathrm{Ni}$ and $^{8}\mathrm{B}+^{208}\mathrm{Pb}$ systems. These calculations demonstrated that CCC can modify the breakup cross sections, with different contributions influencing different angular regions. The nuclear component was found to be particularly sensitive to continuum couplings, while off-diagonal CCC produced a significant reduction in the calculated total breakup cross section for $^{8}\mathrm{B} + ^{58}\mathrm{Ni}$. These findings highlight the importance of including couplings between continuum states when investigating breakup dynamics and demonstrate that their effects may differ between the Coulomb and nuclear contributions.

More recently, the breakup of ^{8}B on the heavier ^{120}Sn target was investigated experimentally at near-barrier energies [17]. Yang et al. measured correlations between the proton and ^{7}Be breakup fragments using a highly efficient silicon detector array. The experimental results were analyzed using CDCC

calculations and revealed distinctive breakup dynamics, including the predominance of elastic breakup in the production of ^{7}Be and the importance of short-lived continuum configurations. The study also highlighted the potential role of Coulomb polarization in the breakup of the proton-halo state. These results provide important information on the breakup of ^{8}B in the presence of a stronger target Coulomb field.

Despite these advances, a systematic comparison of the separate total, Coulomb, and nuclear breakup contributions for ^{8}B + ^{58}Ni and ^{8}B + ^{120}Sn, using a common theoretical framework and examining the influence of CCC on both systems, remains an important problem. These two targets provide a useful basis for investigating the dependence of breakup dynamics on target charge and mass. In particular, the target charge increases from Z_T=28 for ^{58}Ni to Z_T=50 for ^{120}Sn, substantially changing the strength of the Coulomb interaction. Differences in the nuclear interaction, Coulomb barrier, and coupled-channel dynamics may also influence the relative importance of the breakup mechanisms. A systematic comparison can therefore help clarify how target properties affect the Coulomb and nuclear contributions to breakup and how these contributions are modified by continuum-continuum couplings.

In the present work, we employ the Continuum Discretized Coupled Channels (CDCC) method to investigate the total, Coulomb, and nuclear breakup cross sections for the ^{8}B+^{58}Ni and ^{8}B+^{120}Sn reactions at energies above their respective Coulomb barriers. Particular attention is devoted to the effects of continuum-continuum couplings (CCC) by comparing calculations performed with these couplings included and excluded from the coupling matrix elements. This comparison allows us to examine how CCC modify the individual breakup components and how their influence depends on the target nucleus. For the optical potentials adopted in the present calculations, the Coulomb barrier heights are approximately V_B=21.1 MeV for ^{8}B+^{58}Ni [18] and V_B=33.30 MeV for ^{8}B + ^{120}Sn [17]. By comparing the two systems, we aim to establish how the competition between Coulomb and nuclear breakup evolves with target properties and to assess the extent to which continuum-continuum couplings influence this behavior. The elastic scattering angular distributions are compared with available experimental data to assess the reliability of the adopted reaction model. In addition, the contributions of different multipolarities are investigated up to $\lambda_{\max} = 6$ to examine their influence on the reaction dynamics.

2 The Continuum Discretized Coupled Channels (CDCC) method

Details of the continuum discretized coupled channels (CDCC) method can be found in the literature (e.g., Ref. [19]). Since ^{8}B is modelled as a two-body system consisting of a ^{7}Be core and a valence proton, its interaction with the ^{58}Ni and ^{120}Sn targets is treated as a three-body problem within the CDCC

framework. The three-body Hamiltonian can be expressed as follows

$$H_{3B} = -\frac{\hbar^2}{2\mu_{pt}}\nabla^2_{\mathbf{R}} + U_{pt}(\mathbf{r},\mathbf{R}) + \left[-\frac{\hbar^2}{2\mu_{cn}}\nabla^2_r + V_{cn}(\mathbf{r})\right], \tag{1}$$

where μ_{pt} and μ_{cn} denote the projectile-target and core-nucleon reduced masses, respectively. The term $V_{cn}(\mathbf{r})$ represents the interaction potential between the core and the valence nucleon as a function of their relative coordinate $\mathbf{r}$. The potential $U_{pt}(\mathbf{r},\mathbf{R})$ describes the interaction between the projectile and the target, where $\mathbf{R}$ is the coordinate of the projectile-target relative motion. This optical potential is given by

$$\begin{aligned} U_{pt}(\mathbf{r},\mathbf{R}) = &\left[V^N_{ct}(\mathbf{R}_{ct}) + iW_{ct}(\mathbf{R}_{ct})\right] + V^C_{ct}(\mathbf{R}_{ct}) \\ &+ \left[V^N_{nt}(\mathbf{R}_{nt}) + iW_{nt}(\mathbf{R}_{nt})\right] + V^C_{nt}(\mathbf{R}_{nt}), \end{aligned} \tag{2}$$

where the first term represents the core-target interaction, comprising the nuclear potential $V^{\rm nucl}_{ct}(\mathbf{R}_{ct})$, the imaginary potential $W_{ct}(\mathbf{R}_{ct})$, which accounts for the absorption of reaction flux by the target, and the Coulomb potential $V^C_{ct}(\mathbf{R}_{ct})$. Here, $\mathbf{R}_{ct}$ denotes the relative coordinate between the core and the target. Similarly, the second term describes the nucleon-target interaction, including the nuclear potential $V^{\rm N}_{nt}(\mathbf{R}_{nt})$, the imaginary potential $W_{nt}(\mathbf{R}_{nt})$, which accounts for the absorption of reaction flux, and the Coulomb potential $V^C_{nt}(\mathbf{R}_{nt})$. The vector $\mathbf{R}_{nt}$ represents the relative coordinate between the valence nucleon and the target. The Woods-Saxon form factors used to describe the real and imaginary nuclear potentials, as well as the core-nucleon interaction potential, are expressed in the following form

$$V_{WS}(\mathbf{r}) = \left\{V_0 + V_{so}\frac{\mathbf{j}.\mathbf{I}}{r}\frac{d}{dr}\right\}\left[1 + exp\left(\frac{r-R_0}{a_0}\right)\right]^{-1}, \tag{3}$$

where V_0 is the central potential depth, V_{so} is the spin-orbit interaction strength, a_0 is the diffuseness parameter, and R_0 is the radius parameter defining the range of the interaction. The vectors $\mathbf{j}$ and $\mathbf{I}$ denote the relevant angular momentum operators associated with the spin-orbit coupling. In this work, the projectile continuum states are discretized using the binning technique [20, 21], and the three-body CDCC wave function is expanded as follows

$$\Psi^{JM}_{\alpha}(\mathbf{r},\mathbf{R}) = \frac{1}{rR}\sum_{\alpha L}\chi^{LJ}_{\alpha}(R)\mathcal{Y}^{LJ}_{\alpha}(\mathbf{r},\Omega_R), \tag{4}$$

where $\alpha = (i,\ell,s,j)$ represents the set of quantum numbers characterizing the projectile states. Here, $i = 0,1,2,\ldots,N_b$ labels the ground state and the discretized continuum bins, with N_b denoting the total number of bins. The ground-state configuration is specified by $\alpha_0 = (0,\ell_0,s,j_0)$. In this expansion, $\mathcal{Y}^{LJ}_{\alpha}(\mathbf{r},\Omega_R)$ denotes the channel basis function describing the projectile internal state and its coupling to the projectile-target relative motion. The channel basis function is given by the following expression

$$\mathcal{Y}^{LJ}_{\alpha}(\mathbf{r},\Omega_R) = \left[i^L\Phi_{\alpha}(\mathbf{r}) \otimes Y^{\nu}_{L}(\Omega_R)\right]_{JM}, \tag{5}$$

where $\Phi_\alpha(\mathbf{r})$ denotes the projectile internal wave function, constructed from the discretized continuum bin states. It is defined as

$$\Phi_\alpha(\mathbf{r}) = \psi_\alpha(r)\left[i^\ell Y_\ell^\mu \otimes X_s^\lambda\right]_{jm}, \tag{6}$$

where, $\psi_\alpha(r)$ represents the square-integrable radial wave functions associated with the discretized continuum bins, while X_s^λ denotes the projectile spin function obtained by coupling the intrinsic spins of ^{7}Be and the valence proton. By substituting Eq. 4 into the three-body Schrödinger equation, one obtains a set of coupled differential equations governing the radial channel functions $\chi_\alpha^{LJ}(R)$

$$\left(-\frac{\hbar^2}{2\mu_{pt}}\left(\frac{d^2}{dR^2} - \frac{L(L+1)}{R^2}\right) + U_{\alpha_0\alpha_0}^{LJ}(R)+\right)\chi_\alpha^{LJ}(R) + \sum_{\alpha\neq\alpha'} U_{\alpha\alpha'}^{LL'J}(R)\chi_{\alpha'}^{L'J}(R) = [E-\varepsilon_\alpha]\,\chi_\alpha^{LJ}(R), \tag{7}$$

where $U_{\alpha\alpha'}^{LL'J}(R)$, the coupling potentials are defined as follows

$$U_{\alpha\alpha'}^{LL'J}(R) = \left\langle \mathcal{Y}_\alpha^{LJ}(\mathbf{r},\Omega_R)|U_{pt}(\mathbf{r},\mathbf{R})|\mathcal{Y}_{\alpha'}^{L'J}(\mathbf{r},\Omega_R)\right\rangle. \tag{8}$$

Since ^{8}B has no bound excited states, the coupling matrix elements in Eq. 8 can be classified into direct couplings, which connect the ground state ($\alpha = \alpha_0$) to the continuum states, and continuum-continuum couplings (CCC), which include both diagonal ($\alpha = \alpha'$) and off-diagonal ($\alpha \neq \alpha'$) contributions. Furthermore, using the projectile-target interaction defined in Eq. 2, the breakup cross sections can be calculated by considering the total, Coulomb, and nuclear interactions separately. The total breakup cross section accounts coherently for both nuclear and Coulomb interactions, whereas the Coulomb breakup cross section is obtained by retaining only the Coulomb components, $V_{ct}^C + V_{nt}^C$, and the nuclear breakup cross section by retaining only the nuclear components, $V_{ct}^N + V_{nt}^N$. Once the coupling matrix elements have been constructed, the coupled differential equations in Eq. 7 are solved subject to the following boundary conditions

$$\chi_\alpha^{LJ}(R) \overset{R\to\infty}{\to} \frac{i}{2}\left[H_L^-(K_\alpha R)\delta_{\alpha\alpha'} - H_L^+(K_\alpha R)S_{\alpha\alpha'}^J(K_\alpha)\right], \tag{9}$$

where $H_L^\pm(K_\alpha)$ and $S_{\alpha\alpha'}^J(K_\alpha)$ are the Coulomb Hankel functions [22], and the breakup S-matrix from which the breakup observables are derived, with $K_\alpha^2 = 2\mu_{pt}(E-\varepsilon_\alpha)/\hbar^2$.

3 Details of the Numerical Calculation

The projectile nucleus ^{8}B is modelled as a two-body system consisting of a ^{7}Be core and a valence proton ($^8\text{B} \to {}^7\text{Be}+p$). The ground state has an experimental proton separation energy of $\varepsilon_b = 0.137$ MeV [23]. It is described by a proton

in the $0p_{3/2}$ orbital coupled to the $3/2^-$ ground state of the ^{7}Be core, resulting in the ^{8}B ground-state spin and parity of $J^\pi = 2^+$. The Woods-Saxon potential parameters used to generate the bound-state and continuum wave functions are adopted from Ref. [24]. The potential depths are $V_0 = -44.65$ MeV and $V_{\rm so} = -19.59$ MeV·fm^2, while the diffuseness parameters are $a_0 = a_{\rm so} = 0.52$ fm. The corresponding radii are $R_0 = R_{\rm so} = R_C = 2.391$ fm, where V_0 and $V_{\rm so}$ denote the depths of the central and spin-orbit terms of the nuclear potential, respectively; R_0 and $R_{\rm so}$ are their associated radii, and a_0 and $a_{\rm so}$ are the diffuseness parameters. Here, R_C represents the Coulomb radius. The parameters of the ^{7}Be+^{58}Ni and p+^{58}Ni optical potentials were taken from Ref. [25]. Following Ref. [26], the ^{7}Li global optical potential parameters are adopted for the ^{7}Be + ^{120}Sn interaction, while the proton-target potential parameters for $p + ^{120}$Sn are taken from Ref. [27]. For both ^{8}B + ^{58}Ni and ^{8}B + ^{120}Snreactions, the projectile continuum was discretized into energy bins up to $\epsilon_{\rm max} = 9$ MeV. The continuum interval $[0, \epsilon_{\rm max}]$ was discretized using partial wave dependent energy bin widths, with $\Delta\epsilon = 0.5$ MeV for the s- and p-wave continuum states, $\Delta\epsilon = 1.0$ MeV for the d- and f-wave continuum states, $\Delta\epsilon = 1.5$ MeV for the g-wave continuum states, and $\Delta\epsilon = 2.0$ MeV for higher partial waves. Finer energy bins were adopted for the resonant partial waves to provide an adequate description of the resonance contributions. The projectile-target coupling potentials were calculated up to $r_{\rm max} = 200$ fm, while the coupled-channel equations were integrated to a matching radius of $R_{\rm max} = 1000$ fm. The projectile internal angular momentum was included up to $\ell_{\rm max} = 6$, and the multipole expansion of the coupling potentials was truncated at $\lambda_{\rm max} = 6$. The projectile-target relative angular momentum was extended to $L_{\rm max} = 10{,}000$. The CDCC calculations were performed using the FRESCO coupled-channels code [28].

4 Results and Discussion

4.1 Elastic scattering cross sections

Our results are presented in Fig. 1, which shows the differential elastic scattering cross sections normalized to the Rutherford cross section for the ^{8}B + ^{58}Ni reaction at (a) $E_{\rm lab} = 25.3$ MeV and (b) 29.3 MeV, and the ^{8}B + ^{120}Sn reaction at (c) $E_{\rm lab} = 38.7$ MeV and (d) 49.1 MeV. The solid lines represent the full coupling CDCC calculations (CCC), while the triangles denote the experimental data. As shown in Fig. 1, the CDCC calculations, including continuum-continuum couplings (CCC), are in good agreement with the experimental data at forward angles ($\theta \leq 50^\circ$) and backward angles ($\theta \geq 80^\circ$) for (a) $E_{\rm lab} = 25.3$ MeV. For (b) $E_{\rm lab} = 29.3$ MeV, good agreement is observed at $\theta \leq 50^\circ$ and $\theta \geq 70^\circ$. For (c) $E_{\rm lab} = 38.7$ MeV, the calculations reproduce the experimental data well at backward angles ($\theta \geq 120^\circ$), while for (d) $E_{\rm lab} = 49.1$ MeV, the calculated results show good agreement with the experimental data [18,17].

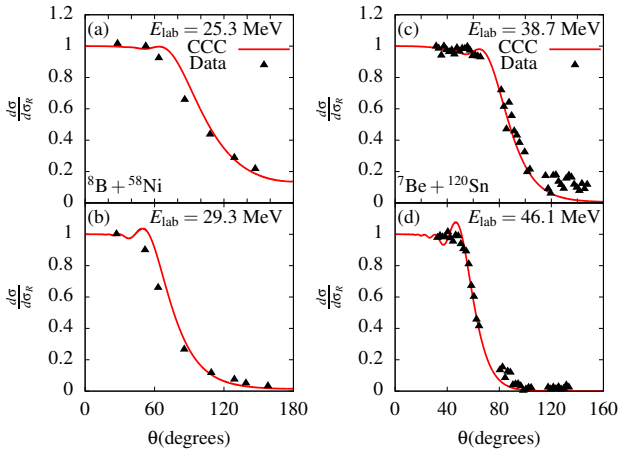


Fig. 1 The differential elastic scattering cross section (ratio to Rutherford cross section) for the ^{8}B+^{58}Ni reaction at (a) $E_{\rm lab} = 25.3$ and (b) 29.3 MeV, and the ^{8}B+^{120}Sn reaction at (c) $E_{\rm lab} = 38.7$ and (d) 49.1 MeV. The solid lines represents the full coupling CDCC calculations (CCC), while the triangles show experimental data. The experimental data are taken from Refs. [18,17].

4.2 Breakup cross sections

To assess the convergence of the total, Coulomb, and nuclear breakup cross sections, we examined their angular distributions as functions of the center-of-mass scattering angle for different values of the maximum continuum bin energy, $\varepsilon_{\rm max} = 2 - 9$ MeV. The calculations were performed for the ^{8}B + ^{58}Ni reaction at $E_{\rm lab} = 26$ MeV (a, c, e) and 31 MeV (b, d, f), and for the ^{8}B+^{120}Sn reaction at $E_{\rm lab} = 41$ MeV (g, i, k) and 49 MeV (h, j, l), as shown in Fig. 2. As shown in Fig. 2, no significant differences are observed among the calculated angular distributions for $\varepsilon_{\rm max}$=2, 3, 4, 5, 6, 8 and 9 MeV, even as the incident energy increases. This indicates that the breakup cross sections exhibit stable convergence with respect to the maximum continuum bin energy over the range investigated. In particular, increasing $\varepsilon_{\rm max}$ beyond these values does not lead to appreciable changes in the calculated angular distributions. As shown in Fig. 3, the differential total (TOT), Coulomb (COU), and nuclear (NUC)breakup cross sections for the ^{8}B + ^{58}Ni reaction are presented at $E_{\rm lab} = 31$ MeV (a, b) and 33 MeV (c, d), while those for the ^{8}B + ^{120}Sn reaction are shown at $E_{\rm lab} = 41$ MeV (e, f) and 49 MeV (g, h). The results with continuum-continuum couplings (CCC) are shown in panels (a), (c), (e), and (g), whereas those without continuum-continuum couplings (NCCC) are presented in panels (b), (d), (f), and (h). In Fig. 3(a) and (c), where all couplings are included, the total and Coulomb breakup cross sections are larger than the nuclear breakup cross section at forward angles ($\theta \leq 60^\circ$). At larger angles, the Coulomb breakup contribution becomes more important. When continuum-continuum couplings are excluded, as shown in Fig. 3(b) and (d),

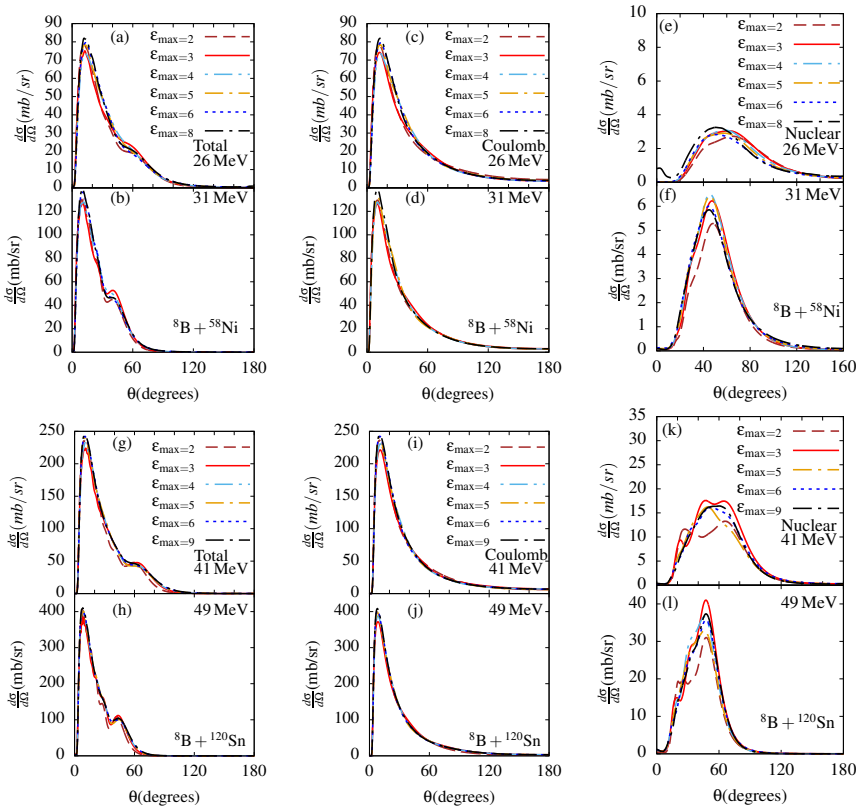


Fig. 2 Convergence of the angular distributions of the total, Coulomb, and nuclear differential breakup cross sections as a function of the center-of-mass scattering angle for different values of the maximum continuum bin energy, $\varepsilon_{\max} = 2 - 9$ MeV, for the $^8\mathrm{B} + {}^{58}\mathrm{Ni}$ reaction at $E_{\mathrm{lab}} = 26$ MeV (a, c, e) and 31 MeV (b, d, f), and for the $^8\mathrm{B} + {}^{120}\mathrm{Sn}$ reaction at $E_{\mathrm{lab}} = 41$ MeV (g, i, k) and 49 MeV (h, j, l).

the total and nuclear breakup cross sections extend to larger scattering angles ($\theta \geq 60°$) for the $^8\mathrm{B} + {}^{58}\mathrm{Ni}$ reaction. As the incident energy increases, the results shown in Fig. 3(e) and (g) indicate that, when continuum-continuum couplings (CCC) are included, the forward angle peaks of the total and Coulomb breakup cross sections decrease from approximately 400 mb to 250 mb, while the peak of the nuclear breakup cross section is suppressed by approximately 30 mb. When CCC are excluded, as shown in Fig. 3(f) and (h), the total breakup cross section exhibits an oscillatory angular distribution, and both the total and nuclear breakup cross sections extend to larger scattering angles for the $^8\mathrm{B} + {}^{120}\mathrm{Sn}$ reaction. These results indicate that CCC substantially reduce the total and nuclear breakup cross sections, whereas the Coulomb breakup cross section is less affected by these couplings, consistent with the findings reported in Ref. [29]. Differential total (TOT), Coulomb (COU), and nuclear (NUC) breakup cross sections for the $^8\mathrm{B} + {}^{58}\mathrm{Ni}$ reaction at $E_{\mathrm{lab}} = 36$ MeV (a,

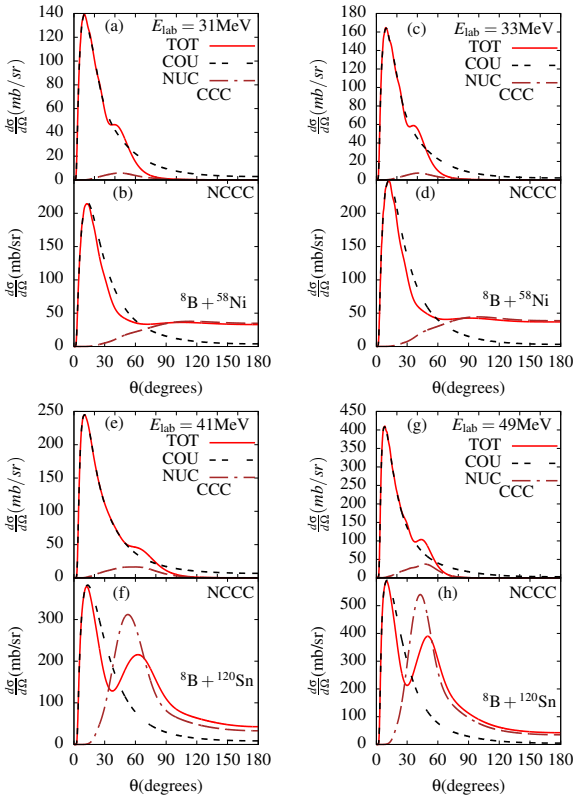


Fig. 3 Differential total (TOT), Coulomb (COU), and nuclear (NUC) breakup cross sections for the $^8\mathrm{B} + {}^{58}\mathrm{Ni}$ reaction at $E_{\mathrm{lab}} = 31$ MeV (a, b) and 33 MeV (c, d), and for the $^8\mathrm{B} + {}^{120}\mathrm{Sn}$ reaction at $E_{\mathrm{lab}} = 41$ MeV (e, f) and 49 MeV (g, h). The results are shown with continuum-continuum couplings (CCC) in panels (a), (c), (e), and (g), and without continuum-continuum couplings (NCCC) in panels (b), (d), (f), and (h).

b) and 41 MeV (c, d), and for the $^8\mathrm{B} + {}^{120}\mathrm{Sn}$ reaction at $E_{\mathrm{lab}} = 58$ MeV (e, f) and 66 MeV (g, h). The results obtained with continuum-continuum couplings (CCC) are shown in panels (a), (c), (e), and (g), while those obtained without continuum-continuum couplings (NCCC) are shown in panels (b), (d), (f), and (h). The results are presented in Fig. 4. From this Fig. 4(a)-(h), the total and nuclear breakup cross sections are substantially reduced by the inclusion of continuum-continuum couplings (CCC), whereas the Coulomb breakup cross section is less affected. These results demonstrate that continuum-continuum couplings (CCC) play an important role in suppressing the angular distributions of the total and nuclear breakup cross sections, while having a comparatively smaller effect on Coulomb breakup cross section, consistent with the findings reported in Refs. [30–32].

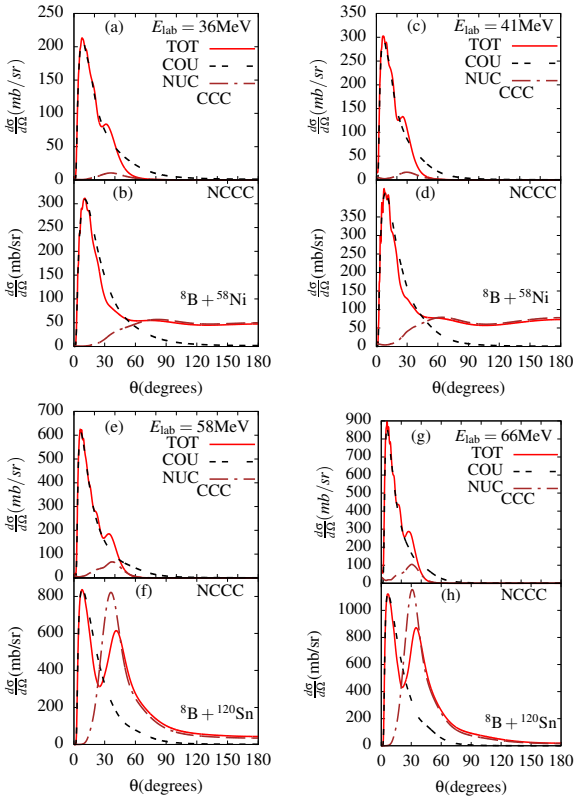


Fig. 4 Differential total (TOT), Coulomb (COU), and nuclear (NUC) breakup cross sections for the $^8B + ^{58}Ni$ reaction at $E_{lab} = 36$ MeV (a, b) and 41 MeV (c, d), and for the $^8B + ^{120}Sn$ reaction at $E_{lab} = 58$ MeV (e, f) and 66 MeV (g, h). The results are shown with continuum-continuum couplings (CCC) in panels (a), (c), (e), and (g), and without continuum-continuum couplings (NCCC) in panels (b), (d), (f), and (h).

4.3 Multipole Contributions

The angular distributions of the total, Coulomb and nuclear differential breakup cross sections as functions of the center-of-mass scattering angle for different multipoles (λ) are presented in Fig. 5. Panels (a)-(f) correspond to the $^8B + ^{58}Ni$ reaction at $E_{lab} = 36$ and 41 MeV, while panels (g)-(l) correspond to the $^8B + ^{120}Sn$ reaction at E_{lab}=58 and 66 MeV. In order to achieve full convergence of the calculated observables, multipoles up to $\lambda = 6$ must be included. To assess the convergence of the CDCC calculations, we compare the results obtained with $\lambda_{max} = 2$ and $\lambda_{max} = 4$. The differences between these calculations indicate that contributions from higher multipoles remain non-negligible. We also present CDCC calculations performed with individual multipoles, namely λ=1, 2, 3 and 5. Interestingly, for both the $^8B + ^{58}Ni$ and

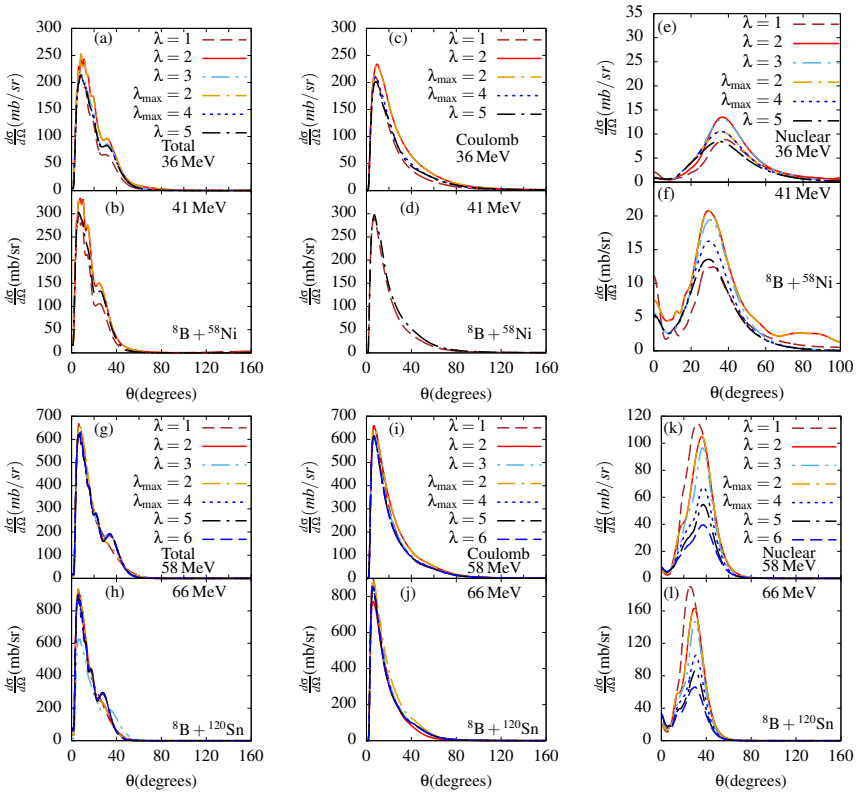


Fig. 5 Angular distributions of the total, Coulomb, and nuclear differential breakup cross sections as functions of the center-of-mass scattering angle for different multipoles (λ). Panels (a)-(f) correspond to the $^8\mathrm{B} + {}^{58}\mathrm{Ni}$ reaction at E_{lab}=36 and 41 MeV, while panels (g)-(l) correspond to the $^8\mathrm{B} + {}^{120}\mathrm{Sn}$ reaction at $E_{\mathrm{lab}} = 58$ and 66 MeV.

$^8\mathrm{B} + {}^{120}\mathrm{Sn}$ reactions, the individual contributions from these multipoles are of comparable magnitude, consistent with the findings reported in Refs. [33,34].

5 Conclusions

The breakup of the weakly bound nucleus ^{8}B has been investigated within the Continuum Discretized Coupled Channels (CDCC) framework for the $^8\mathrm{B} + {}^{58}\mathrm{Ni}$, and $^8\mathrm{B} + {}^{120}\mathrm{Sn}$reactions. The elastic scattering cross section calculations for $^8\mathrm{B} + {}^{58}\mathrm{Ni}$ and $^8\mathrm{B} + {}^{120}\mathrm{Sn}$ show reasonable agreement with the available experimental data over the angular ranges considered, supporting the reliability of the adopted reaction model.

The convergence analysis demonstrates that the calculated total, Coulomb, and nuclear breakup angular distributions exhibit no significant variations for maximum continuum bin energies of $\varepsilon_{\max} = 2$, 3, 4, 5, 6, 8, and 9 MeV. This

indicates that the calculated observables are stable with respect to $\varepsilon_{\max}$ over the investigated range. The multipole analysis further shows that contributions beyond $\lambda_{\max} = 2$ remain non negligible and that multipoles up to $\lambda_{\max} = 6$ are required to achieve convergence within the adopted model space. The individual contributions from $\lambda = 1$, 2, 3, and 5 are of comparable magnitude for both the $^{8}\mathrm{B} + {}^{58}\mathrm{Ni}$ and $^{8}\mathrm{B} + {}^{120}\mathrm{Sn}$ reactions, highlighting the importance of including multiple multipolarities in the CDCC calculations.

The breakup results reveal a strong dependence on the target and the interplay between nuclear and Coulomb interactions. When all couplings are included, the total and Coulomb breakup cross sections exceed the nuclear breakup cross section at forward scattering angles for the $^{8}\mathrm{B} + {}^{58}\mathrm{Ni}$ reaction. The angular distributions also demonstrate that excluding continuum-continuum couplings (CCC) can extend the total and nuclear breakup cross sections to larger scattering angles. For the $^{8}\mathrm{B} + {}^{120}\mathrm{Sn}$ reaction, the forward angle peaks of the total and Coulomb breakup cross sections decrease from approximately 400 mb to 250 mb as the incident energy increases, while the peak nuclear breakup cross section is suppressed by approximately 30 mb when CCC are included. Without CCC, the total breakup angular distribution exhibits pronounced oscillations, and the total and nuclear breakup cross sections extend to larger angles.

In conclusion, the results demonstrate that CCC substantially suppress the total and nuclear breakup cross sections, whereas the Coulomb breakup cross section is comparatively less affected. This behavior is consistent with the findings reported in Refs. [29–32]. The present study provides a systematic investigation of the breakup dynamics of $^{8}\mathrm{B}$ on medium and heavy targets, emphasizing the importance of continuum couplings and multipole contributions in obtaining a reliable description of breakup observables. The results are also consistent with the multipole related findings reported in Refs. [33, 34].

Declarations

- Ethics approval and consent to participate: Not applicable. This study does not involve human participants or animals.
- Consent for publication: Not applicable.
- Availability of data and materials: The data supporting the findings of this study are available from the corresponding author upon reasonable request.
- Competing interests: The author declares that there are no competing interests.
- Funding: This research was supported by the National Research Foundation (NRF) under Grant No. PSTD23031282071.
- Authors' contributions: The author conceived the study, performed the theoretical calculations, analysed the results, and prepared the manuscript. The author read and approved the final manuscript.

– Acknowledgements: The author acknowledges the support provided by the University of South Africa.

References

1. K. Wang *et al.*, *Phys. Lett.* **B** 139957 (2025).
2. I. Tanihata *et al.*, *Phys. Rev. Lett.* **55** 2676 (1985).
3. B. Mukeru, L. V. Ndala and M. L. Lekala, *Int. J. Mo. Phys.* **E 31** 2250025 (2022).
4. B. Mukeru, L. V. Ndala and M. L. Lekala, *Pramana* **95** 106 (2021).
5. B. Mukeru, L. V. Ndala and M. L. Lekala, *Nucl. Phys.* **A 1020** 122397 (2022).
6. L. V. Ndala, *On the study of nuclear reaction mechanisms using exotic nuclei* (PhD diss., University of South Africa 2022).
7. L. V. Ndala and M. L. Lekala, *Nucl. Phys.* **A 1067** 123316 (2026).
8. L. V. Ndala and M. L. Lekala, *Nucl. Phys.* **A 1067** 123317 (2026).
9. L. V Ndala and M. L. Lekala, *EPJ Web Conf.* **378** 02003 (2026).
10. L. V. Ndala and M. L. Lekala, *Braz. J. Phys.* **56** 167 (2026).
11. J. Lubian *et al.*, *Phys. Rev.* **C 79** 064605 (2009).
12. N. Keeley *et al.*, *Prog. Part. Nucl. Phys.* **63** 396 (2009).
13. N. Keeley, R. S. Mackintosh, and C. Beck, *Nucl. Phys.* **A 834** 792c-795c (2010).
14. V. Guimaraes *et al.*, *Phys. Rev. Lett.* **84** 1862 (2000).
15. E. F. Aguilera *et al.*, *Phys. At. Nucl.* **71** 1163-1167 (2008).
16. B. Mukeru, M. L. Lekala, A. S. Denikin, *Nucl. Phys.* **A 935** 18 (2015).
17. L. Yang *et al.*, *Nat. commun.* **13** 7193 (2022).
18. E. F. Aguilera *et al.*, *Phys. Rev.* **C 79** 021601(R) (2009).
19. Austern N *et al.*, *Phys. Rep.* **154** 125 (1987).
20. I. J. Thompson and F. M. Nunes, *Nuclear Reactions for Astrophysics* (Cambridge University Press, New York 2009). See also www.fresco.org.uk
21. J. A. Tostevin, F M Nunes and I. J. Thompson, *Phys. Rev.* **C 63** 024617 (2001).
22. M. Abramowitz and I. A. Stegun I A, *Handbook of Mathematical Functions: with Formulas, Graphs, and Mathematical tables* (Washington, DC: National Bureau of Standards, 1964).
23. W. Wang *et al.*, *Chin. Phys.* **C 41** 030003 (2017). See also at https://www.nndc.bnl.gov/nudat2/
24. G. Goldstein, P. Capel, D. Baye, *Phys. Rev.* **C 76** 024608 (2007).
25. T. L. Belyaeva *et al.*, *Phys. Rev.* **80** 064617 (2009).
26. J. Cook, *Nucl. Phys.* **A 388** 153 (1982).
27. A. J. Koning and J. P. Delaroche, *Nucl. Phys.* **A 713** 231 (2003).
28. I J Thompson *Comput. Phys. Rep.* **7** 167 (1988).
29. B. Mukeru, *J. Phys. G: Nucl. Part. Phys.* **45** 065201 (2018).
30. B. Paes *et al.*, *Nucl. Phys.* **A 890** 1 (2012).
31. F. M. Nunes and I J Thompson, *Phys. Rev.* **C 57** 2818-20 1998.
32. F. M. Nunes and I. J. Thompson, *Phys. Rev.* **C 59** 2652-9 (1999).
33. Y. Kucuk and A. M. Moro, *Phys. Rev. C* **86** 034601 (2012).
34. L. V. Ndala and M. L. Lekala, *Braz. J. Phys.* **56** 235 (2026).